Bulgarian Academy of Sciences
Institute of Mathematics and Informatics
Department of Mathematical Modelling
and Numerical Analysis

NUMERICAL MODELLING OF NONLINEAR BOUNDARY VALUE PROBLEMS OF SECOND AND FOURTH ORDER:

APPLICATION IN PHYSICOCHEMISTRY AND BIOLOGY

Galina Stoyanova Lyutskanova–Zhekova

SUMMARY

of thesis for conferring of academic and scientific degree doctor
in professional field 4.5 Mathematics
(Mathematical modelling and application of mathematics)

SUPERVISORS:

Prof. Dr.Sc. Krassimir D. Danov
Corresponding member of the Bulgarian Academy of Sciences

Assoc. Prof. Ph.D. Ivan B. Bazhlekov

September 2022

The Ph.D. thesis considers three applications of boundary value problems in physico-chemistry and biology:

- to calculate the distribution of the electrostatic potentials in two immiscible fluid phases (polar and nonpolar) and in a dielectric spherical colloidal particle, attached to the flat interface between them;
- to compute the drag force, acting on a spherical colloidal particle, which is attached to a flat interface between two incompressible viscous fluids and translates along it with constant velocity;
- to clarify the effect of interfacial rheology (tangential mobility and immobility of interfaces) on the motion of a long bubble in a narrow cylindrical capillary under the simultaneous action of gravity and Poiseuille flow.

The dissertation is written in English on 160 pages and contains 27 figures and a table. It includes an introduction, three chapters, corresponding to the three applications considered, a conclusion, an appendix, and a bibliography of 142 sources. Three additional materials are attached to the work, which give information on the topics "Tensors in curvilinear coordinates", "Electrostatics" and "Continuum fluid mechanics".

The research, which is described in the thesis, was conducted in the Ph.D. program "Mathematical modeling and application of mathematics" at the department of Mathematical Modelling and Numerical Analysis in the Institute of Mathematics and Informatics, Bulgarian Academy of Sciences.

The dissertation has been discussed and directed for defense at a meeting of an extended unit to the Department of Mathematical Modeling and Numerical Analysis at IMI-BAS, held on 12.09.2022.

The defense of the dissertation will take place on ..... at ..... in auditorium ..... in IMI-BAS at an public meeting of a scientific jury.

The defense materials are available at the library of IMI-BAS.

Contents

1. Introduction

A complex fluid (three-dimensional phase) is fluid, which is not Newtonian or the surface tension on its material interfaces (two-dimensional phases) is not constant. Examples for complex fluids are foams, emulsions, melts, biological cells, tissues and liquids, etc., which have applications in the chemical, pharmaceutical and oil industry, everyday life and medicine. In continuum mechanics, a complex fluid is modelled by the mass, momentum and energy balance equations, which are not closed. To close the physicochemical models and to introduce a mathematical formulation of the respective problems, the natural scientists assume different semi-empirical laws (linear or nonlinear) to relate the stress and strain tensors. Even in the simplest linear rheological case of Newtonian fluids, the Navier–Stokes equations for incompressible fluids become of a fourth order (the elimination of the pressure leads to nonlinear partial differential equations, which contain bi-Laplacian of the velocity vector). For typical applications, the bulk fluids are incompressible but the material interfaces are not — they can deform, take different complex shapes and have considerably different rheological behavior, which is affected by the adsorbed surfactants, polymers or particles, by the properties of the biological membranes, etc. Generally, the appearance of interfaces leads to complex boundary value problems. To construct adequate rheological models, the experimentalists need simplified mathematical models and fast numerical procedures to fit the obtained data and to extract information about the rheological parameters (e.g. the surface dilatational and shear viscosity and elasticity, yield stress, etc.).

In the thesis, we consider three different applications of the boundary value problems in the case of linear or strongly nonlinear models of the second or higher orders. The first problem (Chapter 2) is related to the interaction between large protein molecules and colloid particles (particles of micron or submicron sizes), both of which are attached to the interface between two fluids. For small sizes (below 3 microns), the proteins and colloids (termed as particles) interact with van der Waals, electrostatic and capillary forces. Except for the van der Waals interactions, the electrostatic and capillary forces arise because of the surface charge density of particles and their three-phase contact angles. Due to the small particle volumes, the gravity is negligible and, therefore, the deformation of the interface is a result of the electrostatic pressure distribution along the interface and related to it electro-dipping force. The strategy for computer modeling is to solve the respective problem for flat interface, to calculate the electrostatic pressure distribution and the electro-dipping force; to use the calculated distribution in the normal stress boundary condition in order to compute the interfacial deformation; etc. From experimental viewpoint, the first two steps are the most important.

The second problem (Chapter 3) is a part of two very complex tasks. The first one is to predict the two-dimensional ordering of a large number of molecules and colloidal particles, which float at the surface between two fluids, and the drag forces, which act on them due to their Brownian motion under the action of van der Waals, electrostatic and capillary forces. The second task is related to the fact that there is no direct microscopic method to measure the value of the three-phase contact angle. The recently developed optical trap method uses laser beams to manipulate colloidal particles at the interfaces and biological membranes. From the lateral velocity of a particle and the applied optical tweezer force, the experimentalists measure the drag force of the colloidal particle (tracer). Thus, one needs a fast and precise numerical method to calculate the drag force for a given three-phase contact

angle and to use this procedure for fitting of experimental data in order to obtain the most probable value of the three-phase contact angle.

One of the most difficult problems in physicochemical and biological modeling is to obtain the shape of material interfaces in static and dynamic regimes. The complex shapes, the stability and instability of interfaces and their interactions with other material objects are of general importance for the description of their physicochemical properties. One example is considered in Chapter 4 — a motion of a long bubble through a cylindrical capillary under the action of pressure gradients (Poiseuille flow) and gravity. The bubble surface can be: free, i.e. tangentially mobile interface — classical formulation; tangentially immobile but deformable, e.g. the model of biological membranes, surfactant laden interfaces, etc. The analytical solutions of the classical problems (free surfaces) for the gravity- and for the pressure-driven motion in the case of very small bubble velocity are known as the Bretherton problems [1.1]. The only formulas that extend the validity of the Bretherton formulas and are applicable in the case of bubble with a free surface under the action of pressure, are published in Refs. [1.2, 1.3]. Again, this problem is a part of more complex computations, e.g. a motion of drops and bubbles in a rock porous medium in the oil recovery problems or the motion of biological inclusions in the human veins. Due to the fact that the available numerical calculations are very time consumable, it is difficult (and in the most cases impossible) these calculations to be generalized to complex fluids and material interfaces.

The thesis is organized as follows. The respective problems are described in Chapters 2, 3 and 4, which contain an abstract, literature review, a description of the problem, a method for its solution, detail conclusions and cited references. In fact, these chapters correspond to our publications but do not reproduce them directly. The chapters include detailed mathematical calculations and algorithm descriptions, which are not included in the publications due to the restricted volume. The actuality of the considered problems, new elements in their treatment from physicochemical and mathematical aspects, compared to the available results in the literature, and the main strategies for solving the problems are written in Chapter 5, where our claims are summarized in three points. Finally, because of the possible identical references, cited after different chapters, the list of all used references is added. The thesis contains an appendix and three supplementary materials.

References

[1.1] F. Bretherton, *J. Fluid Mech.* 10, 166–188 (1961).

[1.2] J. Ratulowski, H.-C. Chang, *Phys. Fluids A - Fluid* 1, 1642–1655 (1989).

[1.3] W. Kolb, R. Cerro, *Phys. Fluids A - Fluid* 5, 1549–1567 (1993).

2. Effect of the ionic strength on the electro-dipping force

2.1 Literature overview

The prediction of the properties of dielectric particles at fluid–fluid interfaces is of a crucial importance for the characterization of a particle monolayer, formation of particle-stabilized emulsions, which have a wide application in cosmetics, food industry, biomedical field, etc.

In this chapter, we model a small particle (of radius less than 2–3 microns), attached to the flat interface between water and nonpolar fluid. We assume that there are surface charges at the particle–nonpolar phase boundary [2.1]. In the idealized case of water phase with infinite dielectric permittivity, this problem was solved semi-analytically, using the Mehler–Fock integral transform [2.2]. Our aim in the present study is to analyze the more realistic case of water phase with finite dielectric constant and to calculate the distribution of the electrostatic potentials in all of the phases. The implemented numerical scheme of second order with respect to space and numerical time computes the distribution of the electrostatic potentials in the case of a flat surface, which is an essential step in order to calculate the electro-dipping force.

2.2 Mathematical formulation of the problem

A spherical charged dielectric particle of radius R and dielectric constant $\varepsilon_{\rm p}$ is attached to the interface between nonpolar (oil, air) and water phases with dielectric constants $\varepsilon_{\rm n}$ and $\varepsilon_{\rm w}$, respectively (see Fig. 2.1). The particle position is determined by the three-phase contact angle α and the radius of the three-phase contact line is $r_{\rm c} = R\sin\alpha$. There are no adsorbed charges at the particle–water, $S_{\rm pw}$, and nonpolar–water phase surfaces, $S_{\rm nw}$, while the particle–nonpolar phase interface $S_{\rm pn}$ contains charges of constant surface charge density, $\sigma_{\rm pn}$ [2.3], which induce electrostatic potentials in the volumes.

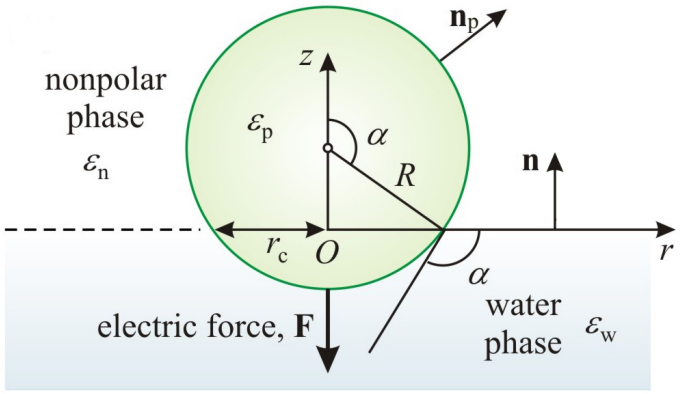

Figure 2.1: Sketch of a particle at the interface between water and nonpolar phases.

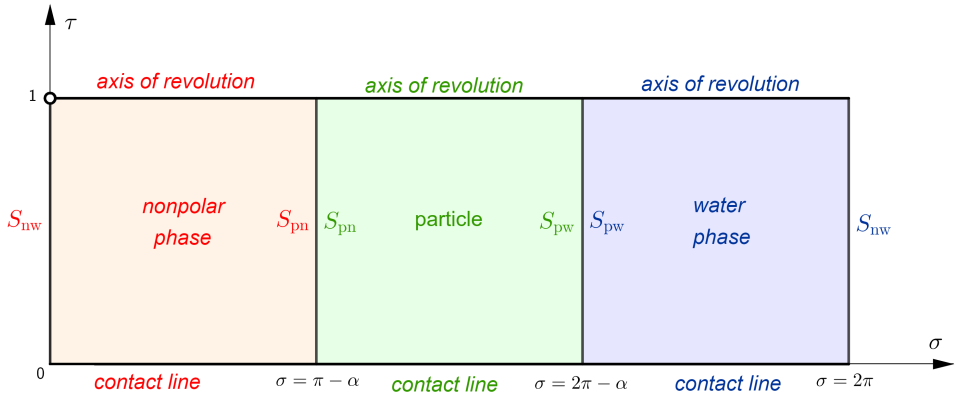

Figure 2.2: Rectangular numerical domains in modified toroidal coordinates.

Then, the dimensionless potentials φ_j, scaled with $r_c\sigma_{\rm pn}/(\varepsilon_0\varepsilon_{\rm n})$, are modelled as solutions of the Laplace equations in the volumes, V_j, i.e.:

$$\nabla^2\varphi_{\rm w} = 0 \text{ in } V_{\rm w},\ \nabla^2\varphi_{\rm n} = 0 \text{ in } V_{\rm n},\ \nabla^2\varphi_{\rm p} = 0 \text{ in } V_{\rm p}, \tag{2.1}$$

where ε_0 is the dielectric permittivity in vacuum, and the subscripts "p", "n" and "w" denote the particle, the nonpolar and water phases, respectively. At the dividing boundaries, we apply the tangential boundary conditions:

$$\varphi_{\rm p} = \varphi_{\rm w} \text{ at } S_{\rm pw},\ \varphi_{\rm p} = \varphi_{\rm n} \text{ at } S_{\rm pn},\ \varphi_{\rm n} = \varphi_{\rm w} \text{ at } S_{\rm nw} \tag{2.2}$$

and the normal boundary conditions

$$\varepsilon_{\rm wn}\mathbf{n}\cdot\nabla\varphi_{\rm w} = \mathbf{n}\cdot\nabla\varphi_{\rm n} \text{ at } S_{\rm nw}, \tag{2.3}$$
$$\varepsilon_{\rm wn}\mathbf{n}_{\rm p}\cdot\nabla\varphi_{\rm w} = \varepsilon_{\rm pn}\mathbf{n}_{\rm p}\cdot\nabla\varphi_{\rm p} \text{ at } S_{\rm pw}, \tag{2.4}$$
$$\varepsilon_{\rm pn}\mathbf{n}_{\rm p}\cdot\nabla\varphi_{\rm p} - \mathbf{n}_{\rm p}\cdot\nabla\varphi_{\rm n} = 1 \text{ at } S_{\rm pn}, \tag{2.5}$$

where $\mathbf{n}_{\rm p}$ is the outer unit normal to the particle surface, $\mathbf{n}$ is the unit normal to $S_{\rm nw}$, pointing at the nonpolar phase, and the dielectric parameters $\varepsilon_{\rm pn}$ and $\varepsilon_{\rm wn}$ are defined as

$$\varepsilon_{\rm pn} = \frac{\varepsilon_{\rm p}}{\varepsilon_{\rm n}},\ \varepsilon_{\rm wn} = \frac{\varepsilon_{\rm w}}{\varepsilon_{\rm n}}. \tag{2.6}$$

Finally, the electrostatic potentials vanish at infinity.

The problem is axissymetric and, therefore, its solution depends only on the axial distance r and axial coordinate z. Thus, the complex dielectric phases domains (Fig. 2.1) are transformed into rectangles (Fig. 2.2) by introducing modified toroidal coordinates τ and σ as follows:

$$r = \frac{1-\tau^2}{h},\ z = \frac{2\tau\sin\sigma}{h},\ h(\tau,\sigma) = 1+\tau^2-2\tau\cos\sigma. \tag{2.7}$$

Then, the positions of the interfaces are $\sigma = 0$ and $\sigma = 2\pi$ from both sides of $S_{\rm nw}$; $\sigma = \pi - \alpha$ at $S_{\rm pn}$; $\sigma = 2\pi - \alpha$ at $S_{\rm pw}$. The axis of revolution corresponds to $\tau = 1$ and the three-phase contact line—to the pole, A_+, where $\tau = 0$.

Using the general formulae for the Laplace operator and directional derivatives in modified toroidal coordinates, we get

$$L_0[\varphi_{\rm w}] = 0,\ L_0[\varphi_{\rm n}] = 0,\ L_0[\varphi_{\rm p}] = 0, \tag{2.8}$$

where the operator L_0 is defined via the formula

$$L_0[\varphi] = \frac{h^3}{4\tau\left(1-\tau^2\right)}\frac{\partial}{\partial\tau}\left[\frac{\tau\left(1-\tau^2\right)}{h}\frac{\partial\varphi}{\partial\tau}\right] + \frac{h^3}{4\tau^2}\frac{\partial}{\partial\sigma}\left(\frac{1}{h}\frac{\partial\varphi}{\partial\sigma}\right). \tag{2.9}$$

At the dividing boundaries $S_{\rm nw}$, $S_{\rm pw}$, $S_{\rm pn}$, the boundary conditions have the form

$$\varphi_{\rm n}|_{\sigma=0} = \varphi_{\rm w}|_{\sigma=2\pi}\,,\ \left.\frac{\partial\varphi_{\rm n}}{\partial\sigma}\right|_{\sigma=0} = \varepsilon_{\rm wn}\left.\frac{\partial\varphi_{\rm w}}{\partial\sigma}\right|_{\sigma=2\pi}, \tag{2.10}$$

$$\varphi_{\rm p}|_{\sigma=2\pi-\alpha} = \varphi_{\rm w}|_{\sigma=2\pi-\alpha}\,,\ \varepsilon_{\rm pn}\left.\frac{\partial\varphi_{\rm p}}{\partial\sigma}\right|_{\sigma=2\pi-\alpha} = \varepsilon_{\rm wn}\left.\frac{\partial\varphi_{\rm w}}{\partial\sigma}\right|_{\sigma=2\pi-\alpha}, \tag{2.11}$$

$$\varphi_{\rm n}|_{\sigma=\pi-\alpha} = \varphi_{\rm p}|_{\sigma=\pi-\alpha}\,,\ \left.\frac{\partial\varphi_{\rm n}}{\partial\sigma}\right|_{\sigma=\pi-\alpha} - \varepsilon_{\rm pn}\left.\frac{\partial\varphi_{\rm p}}{\partial\sigma}\right|_{\sigma=\pi-\alpha} = \frac{2\tau}{h}. \tag{2.12}$$

Due to the axial symmetry of the problem, the following boundary conditions:

$$\left.\frac{\partial\varphi_{\rm n}}{\partial\tau}\right|_{\tau=1} = \left.\frac{\partial\varphi_{\rm p}}{\partial\tau}\right|_{\tau=1} = \left.\frac{\partial\varphi_{\rm w}}{\partial\tau}\right|_{\tau=1} = 0 \tag{2.13}$$

are added at the axis of revolution. At the pole A_+, the potentials are defined to be zero

$$\varphi_{\rm n} = \varphi_{\rm p} = \varphi_{\rm w} = 0 \text{ for } \tau = 0 \tag{2.14}$$

due to linearity of the problem. The physical potentials are computed by subtracting from the dimensionless φ_l their value at infinity.

2.3 Asymptotic behaviour of the model at the three-phase contact line

To compute the electro-dipping force with high accuracy, we investigate the asymptotic behaviour of the model equations in the close vicinity of the three-phase contact line (for $\tau \to 0$). Thus, we search for the solution of the problem (2.8)– (2.12) in the form

$$\varphi_i = \tau^\nu\left[A_i^c\cos(\nu\sigma) + A_i^s\sin(\nu\sigma)\right],\ i = {\rm n},\ {\rm p},\ {\rm w}, \tag{2.15}$$

where $0.5 < \nu < 1$ and A_i^c and A_i^s are unknown constants. The substitution of these solutions into the boundary conditions (2.10)– (2.12) leads to a homogeneous system of six linear equations for A_i^c and B_i^c. This system has a nontrivial solution, when its determinant is equal to zero. Thus, we arrive to the following equation for the singularity parameter, ν:

$$\begin{aligned}&\frac{2\varepsilon_{\rm pn}(1-\varepsilon_{\rm wn})^2}{(1+\varepsilon_{\rm pn})(1+\varepsilon_{\rm wn})(\varepsilon_{\rm pn}+\varepsilon_{\rm wn})} - \sin^2(\nu\pi) = \\ &\frac{(1-\varepsilon_{\rm pn})(1-\varepsilon_{\rm wn})}{(1+\varepsilon_{\rm pn})(1+\varepsilon_{\rm wn})}\cos^2(\nu\alpha) + \frac{(1-\varepsilon_{\rm wn})(\varepsilon_{\rm pn}-\varepsilon_{\rm wn})}{(1+\varepsilon_{\rm wn})(\varepsilon_{\rm pn}+\varepsilon_{\rm wn})}\cos^2\left[\nu(\pi-\alpha)\right].\end{aligned} \tag{2.16}$$

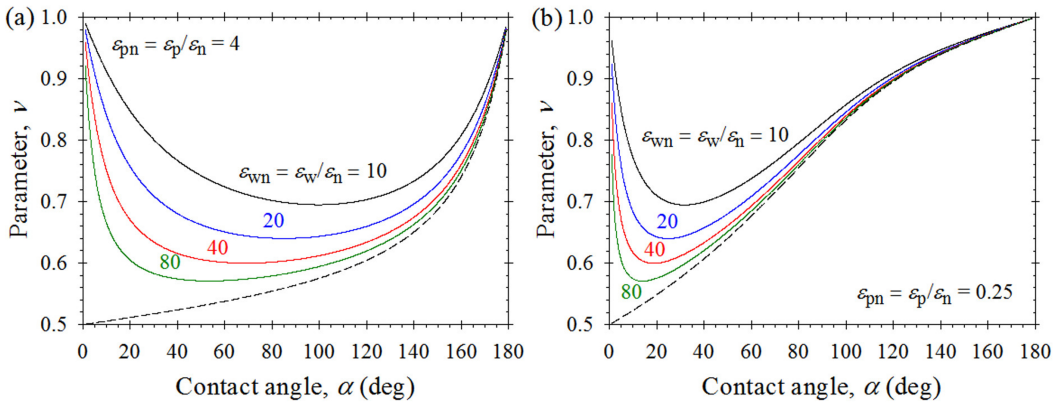

Figure 2.3: Dependence of singularity parameter ν on the contact angle α and ratio $\varepsilon_{\rm wn}$: (a) $\varepsilon_{\rm pn} = 4$; (b) $\varepsilon_{\rm pn} = 0.25$. Dashed lines show the idealized case, studied in [2.2].

The solutions of equation (2.16) for two different ratios $\varepsilon_{\rm pn}$ at different values of $\varepsilon_{\rm wn}$ are shown in Fig. 2.3. When $\varepsilon_{\rm wn} \to \infty$, from (2.16) it follows the model case, studied in [2.2]. The singularity in the model case, depicted with dashed lines in Fig. 2.3, is stronger than that in all other cases. Moreover, the values of ν increase with the decrease of the ratio between dielectric constants of water and nonpolar phase, $\varepsilon_{\rm wn}$. This effect is more pronounced for larger values of $\varepsilon_{\rm wn}$ and more hydrophilic particles.

2.4 Numerical method

Instead of solving the considered elliptical problem, we introduce numerical time t and solve the following parabolic problem:

$$\frac{\partial \varphi_l}{\partial t} = T\left[\varphi_l\right] + S[\varphi_l],\ \varphi_l \in V_l,\ 0 < t \le T,\ l = \text{n, p, w}, \tag{2.17}$$

$$\varphi_l(\tau, \sigma, 0) = \varphi_{l0}(\tau, \sigma),\ l = \text{n, p, w} \tag{2.18}$$

with applied boundary conditions (2.10)– (2.14), where $T[.]$ and $S[.]$ are the following operators:

$$T[\varphi] = \frac{h\tau}{1-\tau^2}\frac{\partial}{\partial \tau}\left[\frac{\tau(1-\tau^2)}{h}\frac{\partial \varphi}{\partial \tau}\right],\ S[\varphi] = h\frac{\partial}{\partial \sigma}\left(\frac{1}{h}\frac{\partial \varphi}{\partial \sigma}\right). \tag{2.19}$$

We introduce a mesh $\omega = \omega_\tau \times (\omega_{\rm n} \cup \omega_{\rm p} \cup \omega_{\rm w}) \times \omega_t$, where ω_τ, $\omega_{\rm n}$, $\omega_{\rm p}$, $\omega_{\rm w}$, ω_t are defined as

$$\omega_\tau = \{\tau_i = i\delta_\tau,\ \delta_\tau = 1/N,\ i = 0, 1, \cdots, N\}, \tag{2.20}$$

$$\omega_{\rm n} = \{\sigma_{{\rm n},j} = j\delta_{\rm n},\ \delta_{\rm n} = (\pi - \alpha)/N_{\rm n},\ j = 0, 1, \cdots, N_{\rm n}\}, \tag{2.21}$$

$$\omega_{\rm p} = \{\sigma_{{\rm p},j} = \pi - \alpha + j\delta_{\rm p},\ \delta_{\rm p} = \pi/N_{\rm p},\ j = 0, 1, \cdots, N_{\rm p}\}, \tag{2.22}$$

$$\omega_{\rm w} = \{\sigma_{{\rm w},j} = 2\pi - \alpha,\ j\delta_{\rm w},\ \delta_{\rm w} = \alpha/N_{\rm w},\ j = 0, 1, \cdots, N_{\rm w}\}, \tag{2.23}$$

$$\omega_t = \{t_k = k\delta_t,\ \delta_t = T/M,\ k = 0, 1, \cdots, M\}. \tag{2.24}$$

Let us denote the approximate solution of the considered problem at a point $(\tau_i, \sigma_{l,j}, t_k)$ by $\phi_l|_{ij}^k$, l =n, p, w, the standard second-order approximations of the differential operators S

and T by $\tilde{S}$ and $\tilde{T}$, and

$$\delta\phi_l|_{ij}^{k+1} = \phi_l|_{ij}^{k+1} - \phi_l|_{ij}^{k}\,,\ l = \text{n, p, w}. \tag{2.25}$$

We solve the problem (2.17)–(2.18), (2.10)– (2.14), using the D'Yakonov method, which belongs to the class of alternating direction implicit methods (ADIM). First, one solves

$$\left(U - \frac{\delta_t}{2}\tilde{S}\right)\left[\psi_l|_{ij}^{k+1}\right] = \delta_t\tilde{T}\left[\phi_l|_{ij}^{k}\right] + \delta_t\tilde{S}\left[\phi_l|_{ij}^{k}\right],\ l = \text{n, p, w} \tag{2.26}$$

with appropriate boundary conditions, applied for $\psi_l|_{ij}^{k+1}$ at the particle surface and at the fluid-fluid interface. Then, one solves the system:

$$\left(U - \frac{\delta_t}{2}\tilde{T}\right)\left[\delta\phi_l|_{ij}^{k+1}\right] = \psi_l|_{ij}^{k+1},\ l = \text{n, p, w} \tag{2.27}$$

with respective boundary conditions, applied for $\delta\phi_l|_{ij}^{k+1}$ at the three-phase contact line and at the axis of revolution. Finally, $\phi_l|_{ij}^{k+1}$ is obtained, using Eq. (2.25).

The main issue in the ADIM arises from the complexity of the boundary conditions. In order to have a second-order scheme with respect to t, one should take a special care of the form of the boundary conditions. The boundary conditions at the particle surface, at the fluid–fluid interface and at the axis of revolution are obtained by extending the definition of the operators S and T to hold on the dividing boundaries, assuming the validity of the Laplace equations in their close vicinity. The boundary conditions at the three-phase contact line are approximated directly. At the axis of revolution, we replace the boundary conditions (2.13) with equations (2.27), in which S and T are approximated by

$$\tilde{S}[\phi_l|_{Nj}^{k}] = \frac{1-\cos\sigma_j}{\delta_\sigma^2}\cdot\left[\frac{\phi_l|_{N,j+1}^{k} - \phi_l|_{N,j}^{k}}{1-\cos\sigma_{j+1/2}} - \frac{\phi_l|_{N,j}^{k} - \phi_l|_{N,j-1}^{k}}{1-\cos\sigma_{j-1/2}}\right],\ j = \overline{1, N_l-1}, \tag{2.28}$$

$$\tilde{T}[\phi_l|_{Nj}^{k}] = \frac{-7\,\phi_l|_{Nj}^{k} + 8\,\phi_l|_{N-1,j}^{k} - \phi_l|_{N-2,j}^{k}}{\delta_\tau^2},\ j = \overline{1, N_l-1}. \tag{2.29}$$

Next, the normal boundary condition (2.10) is replaced by equation (2.26), in which one approximates the operators T and S by

$$\begin{aligned}\tilde{T}[\phi_{\text{n}}|_{i0}^{k}] = {}& \frac{\tau_i(1-\tau_i)}{\delta_\tau(1+\tau_i)}\cdot\left[\frac{\tau_{i+1/2}(1+\tau_{i+1/2})}{1-\tau_{i+1/2}}\cdot\frac{\phi_{\text{n}}|_{i+1,0}^{k} - \phi_{\text{n}}|_{i,0}^{k}}{\delta_\tau}\right.\\ & \left. - \frac{\tau_{i-1/2}(1+\tau_{i-1/2})}{1-\tau_{i-1/2}}\cdot\frac{\phi_{\text{n}}|_{i,0}^{k} - \phi_{\text{n}}|_{i-1,0}^{k}}{\delta_\tau}\right],\end{aligned} \tag{2.30}$$

$$\begin{aligned}\tilde{S}[\phi_{\text{n}}|_{i0}^{k}] = {}& \frac{1}{\delta_{\text{n}} + \varepsilon_{\text{wn}}\delta_{\text{w}}}\cdot\frac{-7\,\phi_{\text{n}}|_{i0}^{k} + 8\,\phi_{\text{n}}|_{i1}^{k} - \phi_{\text{n}}|_{i2}^{k}}{2\delta_{\text{n}}}\\ & + \frac{\varepsilon_{\text{wn}}}{\delta_{\text{n}} + \varepsilon_{\text{wn}}\delta_{\text{w}}}\cdot\frac{-7\,\phi_{\text{w}}|_{iN_{\text{w}}}^{k} + 8\,\phi_{\text{w}}|_{i,N_{\text{w}}-1}^{k} - \phi_{\text{w}}|_{i,N_{\text{w}}-2}^{k}}{2\delta_{\text{w}}},\ i = \overline{0, N}.\end{aligned} \tag{2.31}$$

The normal boundary conditions (2.11) and (2.12) are approximated analogously.

Because of the boundary conditions, the linear system in the τ-direction is described by a pentadiagonal matrix. Due to the periodicity of the solution at S_{nw}, the respective matrix of the system in the σ-direction is a pentadiagonal with two additional non-zero elements at the end of its first row and at the beginning of its last row. We developed a direct elimination numerical method to solve a linear system of the considered type.

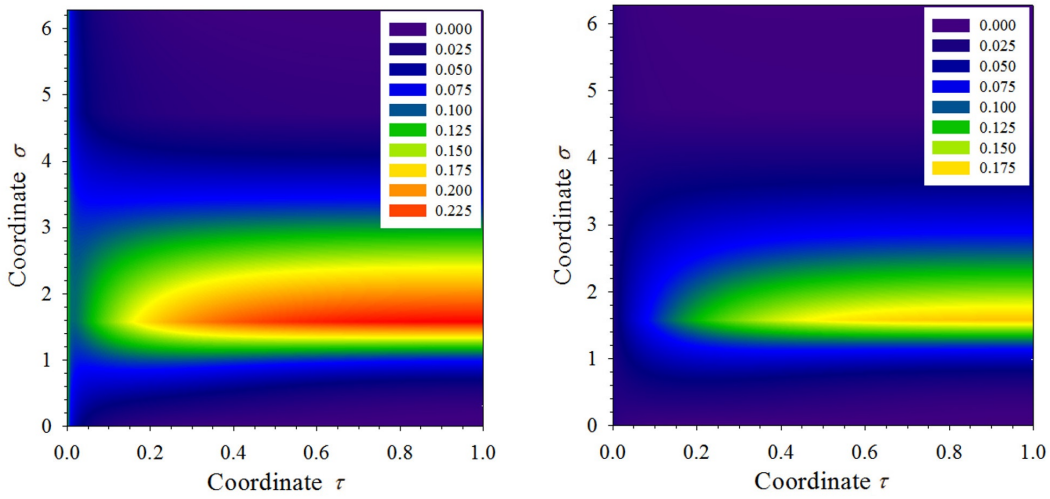

(a) $\varepsilon_{\rm pn} = 0.874$ and $\varepsilon_{\rm wn} = 17.2$ (b) $\varepsilon_{\rm pn} = 2$ and $\varepsilon_{\rm wn} = 40$

Figure 2.4: Distribution of the electrostatic potentials for $\alpha = 90°$.

2.5 Numerical results

To achieve good precision of the numerical calculations, we discretize each numerical domain by introducing a 100×100 uniform mesh. The time step δ_t is set to the minimum of δ_τ, $\delta_{\rm n}$, $\delta_{\rm p}$ and $\delta_{\rm w}$. The CPU time for computation of the potential distributions on a laptop with processor Intel Core i5-4200H is less than a second for any contact angle $\alpha \in (0°, 180°)$.

Figs. 2.4b and 2.5b correspond to experimental system parameters $\varepsilon_{\rm pn} = 2$ and $\varepsilon_{\rm wn} = 40$ [2.1] and Figs. 2.4a and 2.5a — to the system parameters $\varepsilon_{\rm pn} = 0.874$ and $\varepsilon_{\rm wn} = 17.2$.

Fig. 2.4 shows the distribution of the physical potentials in the numerical domains for three-phase contact angle $\alpha = 90°$. The considerably higher dimensionless potentials are obtained for larger values of the dielectric constant of the nonpolar phase. At the coordinate lines, $\sigma = 0$ ($S_{\rm nw}$) and $\sigma = 3\pi/2$ ($S_{\rm pw}$), the electrostatic potentials are considerably lower than those at coordinate line $\sigma = \pi/2$ ($S_{\rm pn}$). As it can be expected, the maxima of the electrostatic potentials are at the cross-section of the particle–nonpolar interface and the axis of revolution. In both cases, the dielectric constant of water is so high that the water phase suppresses the penetration of the electric field in polar phase.

The calculations in [2.1, 2.2] are performed, assuming zero values of the potentials at the boundaries of the polar fluid. The magnitude of the electro-dipping force decreases if the electrostatic potentials at these boundaries are different than zero. Fig. 2.5 shows the distribution of the surface potentials along the boundaries (solid lines correspond to $S_{\rm pn}$; dashed lines — to $S_{\rm pw}$; dot–dashed lines — to $S_{\rm nw}$). The increase in the three-phase contact angle (more hydrophobic particles) leads to higher potentials because there are more charges, adsorbed at the particle–nonpolar fluid interface. It is important to note that the surface potentials at the particle–water boundary are different from zero. Thus, the boundary $S_{\rm pw}$ also contributes to the electro-dipping force. For $\alpha = 45°$ and $\alpha = 90°$, this contribution is small, while for $\alpha = 135°$—it is not negligible. Increasing dielectric constant of the nonpolar phase $\varepsilon_{\rm n}$, the electrostatic potential at boundary $S_{\rm pw}$ increases.

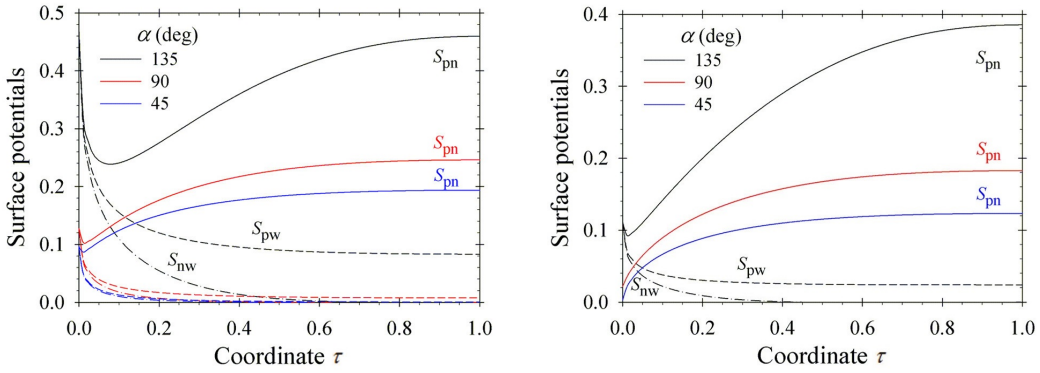

(a) $\varepsilon_{pn} = 0.874$ and $\varepsilon_{wn} = 17.2$ (b) $\varepsilon_{pn} = 2$ and $\varepsilon_{wn} = 40$

Figure 2.5: Distribution of potentials along the interfaces for $\alpha = 45°$, $\alpha = 90°$ and $\alpha = 135°$.

2.6 Conclusion

The proposed effective numerical algorithm, based on the ADIM, enables us to do fast and precise calculation of the electrostatic distributions, generated from a charged dielectric particle, attached to the nonpolar–water interface. For faster calculations, we transform the complex dielectric phase domains into rectangles, using a modification of the toroidal coordinates. The resulting systems in the respective directions of ADIM are solved, using a direct elimination method.

The numerical results show the effect of the three-phase contact angle and the dielectric properties on the induced electric fields and the magnitude of the electro-dipping force. Generally, the decrease of the ratios of the dielectric constants of the particle and nonpolar phase, $\varepsilon_p/\varepsilon_n$, and that of water and nonpolar phase, $\varepsilon_w/\varepsilon_n$, leads to the more pronounced penetration of the electric field and higher surface potentials at the particle–water and nonpolar fluid–water boundaries. The magnitude of the potentials is larger for more hydrophobic particles. The calculations generalize known results — the idealized case of a thin electric double layer in water [2.1], where the dielectric constants of the particle and the nonpolar phase are assumed to be negligible with respect to the constant of water, and the idealized case of water phase with infinite dielectric permittivity [2.2].

References

[2.1] K. Danov, P. Kralchevsky, M. Boneva, *Langmuir* 20, 6139–6151 (2004).
[2.2] K. Danov, P. Kralchevsky, *J. Colloid Interface Sci.* 298, 213–231 (2006).
[2.3] T. Horozov, R. Aveyard, J. Clint, B. Binks, *Langmuir* 19, 2822–2829 (2003).

3. Motion of a spherical particle, attached to the interface between two viscous fluids

3.1 Literature overview

The two-dimensional layers of micro- and nano-particles, attached to interfaces, are related to the production of antireflective surface coverages in solar panels, charge-coupled devices, and bio-memory chips. The quality of these layers depends on the values of the contact angle, α, and the mobility of particles at the interfaces. For small particles, α is measured from the translational motion of individual particles, attached to fluid–fluid interfaces.

In the current work, we calculate the drag coefficient of a spherical particle, located at a flat interface between two viscous fluids and moving parallel to it. If one of the fluid phases is air, the problem has a semi-analytical solution in terms of the Mehler–Fock integral transformation [3.1], which is valid only for particles more immersed in the fluid phase ($\alpha \leq 90°$). The general problem is solved in [3.2], using the two-vorticity-one-velocity formalism. A major drawback of the proposed method in [3.2] is that it is slow. In the present study, we develop a fast and effective numerical method for the general problem, applying the gauge method. This algorithm is needed in order to determine experimentally the contact angle of micron particles and to solve the two-dimensional crystallization problem.

3.2 Mathematical formulation of the problem

A small spherical particle of radius R is attached to the interface between two infinite incompressible viscous fluids and moves parallel to it with known constant velocity V (see Fig. 3.1). For small capillary numbers, the perturbations of the dividing surface due to the particle motion are sufficiently small so that the surface is flat. Thus, the three-phase contact line is a circumference of radius $r_c = R\sin\alpha$, where α is the three-phase contact angle. The center of the three-phase contact line is chosen to be an origin of a Cartesian coordinate system with unit basis vectors $\mathbf{e}_x$, $\mathbf{e}_y$, and $\mathbf{e}_z$, where $\mathbf{e}_y$ points at the direction of the particle movement and $\mathbf{e}_z$ is the unit normal to the fluid–fluid interface, pointing at the upper fluid phase (see Fig. 3.1).

The translation of the particle causes the fluid motion, which is so slow that the inertia terms in the Navier–Stokes equations can be neglected. Then, the dimensionless local velocity $\mathbf{v}_m$ (scaled with V) in the fluid volume V_m is described as a solution of the Stokes equation, i.e.:

$$\nabla \cdot \mathbf{v}_m = 0 \text{ in } V_m,\ \nabla p_m = \nabla^2 \mathbf{v}_m \text{ in } V_m,\ m = 1, 2, \tag{3.1}$$

where η_m is the dynamic viscosity, p_m is the dimensionless pressure (scaled with $\eta_m V/r_c$) and subscripts "1" and "2" denote the upper and lower phases, respectively.

In order to close the problem, we apply the no-slip boundary conditions at the particle surface, S_p:

$$\mathbf{v}_m = \mathbf{e}_y \text{ at } S_\mathrm{p},\ m = 1, 2, \tag{3.2}$$

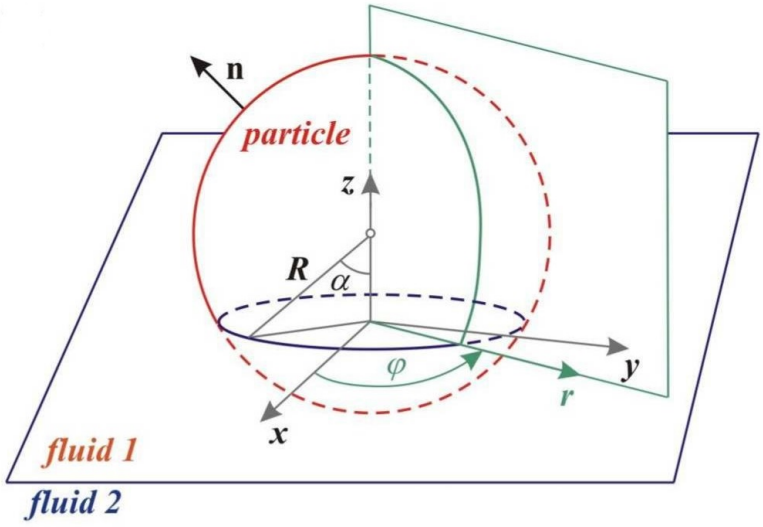

Figure 3.1: Sketch of a spherical particle, attached to the plane interface between two fluids.

the kinematic and the dynamic boundary conditions at the non-perturbed interface $z = 0$:

$$\mathbf{v}_1 = \mathbf{v}_2,\ \mathbf{v}_1 \cdot \mathbf{e}_z = 0,\ \mathbf{v}_2 \cdot \mathbf{e}_z = 0 \text{ at } z = 0, \tag{3.3}$$

$$\mu_1 \frac{\partial \mathbf{v}_1}{\partial z} \times \mathbf{e}_z = \mu_2 \frac{\partial \mathbf{v}_2}{\partial z} \times \mathbf{e}_z \text{ at } z = 0, \tag{3.4}$$

where the dimensionless viscous coefficients are given by $\mu_m = \eta_m/(\eta_1 + \eta_2),\ m = 1, 2$. Finally, the physical values of $\mathbf{v}_m$ and p_m in both phases vanish at large distances from the particle.

Next, one transforms the model into a form, which is convenient for numerical modelling. First, the problem is reformulated, using the gauge method:

$$\mathbf{v}_m = \mathbf{w}_m - \nabla \xi_m,\ p_m = -\nabla^2 \xi_m,\ m = 1, 2. \tag{3.5}$$

Its main idea is to transform the original system, which consists of six second-order and two first-order partial differential equations, into one — of eight elliptic partial differential equations. Second, we simplify the three-dimensional problem to the two-dimensional one, taking into account the fact that the considered problem contains only the first mode with respect to the Fourier transform:

$$w_{mr} = a_{mr} \sin\varphi,\ w_{m\varphi} = a_{m\varphi} \cos\varphi,\ w_{mz} = a_{mz} \sin\varphi,\ \xi_m = b_m \sin\varphi,\ m = 1, 2. \tag{3.6}$$

Next, the partial differential equations in the system are uncoupled by introducing the following new variables:

$$u_{m0} = \frac{a_{mr} + a_{m\varphi}}{4},\ u_{m1} = \frac{a_{mz}}{2},\ u_{m2} = \frac{a_{mr} - a_{m\varphi}}{4},\ b_{m1} = b_m - \frac{r a_{mr} + z a_{mz}}{2} \tag{3.7}$$

for $m = 1, 2$. In order to transform the complex geometry of the problem into rectangles, we use the modification of the toroidal coordinates (2.7). Finally, one obtains the following

problem in terms of the new functions, u_{mj} and b_{m1}, ($m = 1, 2$ and $j = 0, 1, 2$):

$$L_0[u_{m0}] = 0,\ L_1[u_{m1}] = 0,\ L_2[u_{m2}] = 0,\ L_1[b_{m1}] = 0,\ m = 1, 2, \tag{3.8}$$

where $L_n[u]$ are defined as

$$L_n[u] = \frac{h^3}{4\tau\left(1-\tau^2\right)}\frac{\partial}{\partial\tau}\left[\frac{\tau\left(1-\tau^2\right)}{h}\frac{\partial u}{\partial\tau}\right] + \frac{h^3}{4\tau^2}\frac{\partial}{\partial\sigma}\left(\frac{1}{h}\frac{\partial u}{\partial\sigma}\right) - \frac{n^2h^2}{\left(1-\tau^2\right)^2}u. \tag{3.9}$$

The respective boundary conditions are applied to the problem:

- **Boundary conditions at the upper ($\sigma = \alpha$) or at lower part of the particle surface ($\sigma = \alpha - \pi$):**

$$2\left[\left(1+\tau^2\right)\cos\sigma - 2\tau\right]u_{m2} + \left[\left(1-\tau^2\right)\sin\sigma\right]u_{m1} = 0,\ m = 1, 2; \tag{3.10}$$

$$u_{m2} + \frac{\left(1-\tau^2\right)\sin\sigma}{8\tau}\frac{\partial}{\partial\sigma}\left[b_{m1} + \frac{1-\tau^2}{h}(u_{m0}+u_{m2}) + \frac{2\tau\sin\sigma}{h}u_{m1}\right] = 0,\ m = 1, 2; \tag{3.11}$$

$$u_{m0} - u_{m2} = \frac{1}{2},\ b_{m1} + \frac{1-\tau^2}{h}(u_{m0}+u_{m2}) + \frac{2\tau\sin\sigma}{h}u_{m1} = 0,\ m = 1, 2; \tag{3.12}$$

- **Boundary conditions at the fluid–fluid interface ($\sigma = 0$):**

$$u_{10} = u_{20},\ u_{12} = u_{22},\ b_{11} = b_{21},\ m = 1, 2; \tag{3.13}$$

$$u_{m1} - \frac{(1-\tau)^2}{2\tau}\frac{\partial b_{m1}}{\partial\sigma} - \frac{1-\tau^2}{2\tau}\frac{\partial}{\partial\sigma}(u_{m0}+u_{m2}) = 0,\ m = 1, 2; \tag{3.14}$$

$$\mu_1\frac{\partial u_{10}}{\partial\sigma} = \mu_2\frac{\partial u_{20}}{\partial\sigma},\ \mu_1\frac{\partial u_{12}}{\partial\sigma} = \mu_2\frac{\partial u_{22}}{\partial\sigma},\ \mu_1\frac{\partial b_{11}}{\partial\sigma} = \mu_2\frac{\partial b_{21}}{\partial\sigma},\ m = 1, 2; \tag{3.15}$$

- **Boundary conditions at the axis of revolution ($\tau = 1$):**

$$\frac{\partial u_{m0}}{\partial\tau} = 0,\ u_{m1} = 0,\ u_{m2} = 0,\ b_{m1} = 0,\ m = 1, 2; \tag{3.16}$$

- **Boundary conditions at the three-phase contact line ($\tau = 0$):**

$$u_{m2} = \frac{1}{8}\left(\frac{\partial b_m}{\partial\tau}\cos\sigma - \frac{\partial^2 b_m}{\partial\sigma\partial\tau}\sin\sigma\right),\ m = 1, 2, \tag{3.17}$$

$$u_{m1} = \frac{1}{4}\left(\frac{\partial b_m}{\partial\tau}\sin\sigma + \frac{\partial^2 b_m}{\partial\sigma\partial\tau}\cos\sigma\right),\ m = 1, 2, \tag{3.18}$$

$$u_{m0} = u_{m2} + \frac{1}{2},\ b_{m1} = -u_{m0} - u_{m2},\ m = 1, 2, \tag{3.19}$$

where b_m is defined as

$$b_m(\tau, \sigma) = b_{m1} + \frac{1-\tau^2}{h}\left(u_{m0}+u_{m2}\right) + \frac{2\tau\sin\sigma}{h}u_{m1},\ m = 1, 2; \tag{3.20}$$

- **Boundary conditions at infinity ($\tau = 1,\ \sigma = 0$):**

$$u_{m0}(1, 0) = u_{m1}(1, 0) = u_{m2}(1, 0) = b_{m1}(1, 0) = 0,\ m = 1, 2. \tag{3.21}$$

3.3 Asymptotic behaviour of the model at the three-phase contact line

In order to have a good approximation for the drag coefficient, we investigate the asymptotic behaviour of the model in the close vicinity of the three-phase contact line (for $\tau \to 0$). Analogously to the computations in the Chapter 2, we obtain the following equation for the singularity parameter λ:

$$\mu_1 \left[\sin(2\lambda\alpha) - \lambda \sin(2\alpha)\right] \left\{\cos[2\lambda(\alpha-\pi)] - \lambda^2 \cos(2\alpha) + \lambda^2 - 1\right\} = \mu_2 \left\{\sin[2\lambda(\alpha-\pi)] - \lambda \sin(2\alpha)\right\} \left[\cos(2\lambda\alpha) - \lambda^2 \cos(2\alpha) + \lambda^2 - 1\right]. \tag{3.22}$$

The pressure function has a stronger than logarithmic singularity inside the regions, shown in Fig. 3.2, where the singularity parameter $\lambda_p := \lambda - 1$ is in the interval $(-0.5, 0)$. Fig. 3.2 depicts the dependence of λ_p on the three-phase contact angle, α, and viscosity ratio, μ_1. Because of the symmetry, the picture is analogous to that, obtained by replacing μ_1 with μ_2 and α with $\pi - \alpha$. One sees that the pressure singularity becomes stronger with the decrease of viscosity ratio μ_1. Due to the fact $\lambda_p > -0.5$, the singularity is weak and the drag force, as well as the drag coefficient, are finite.

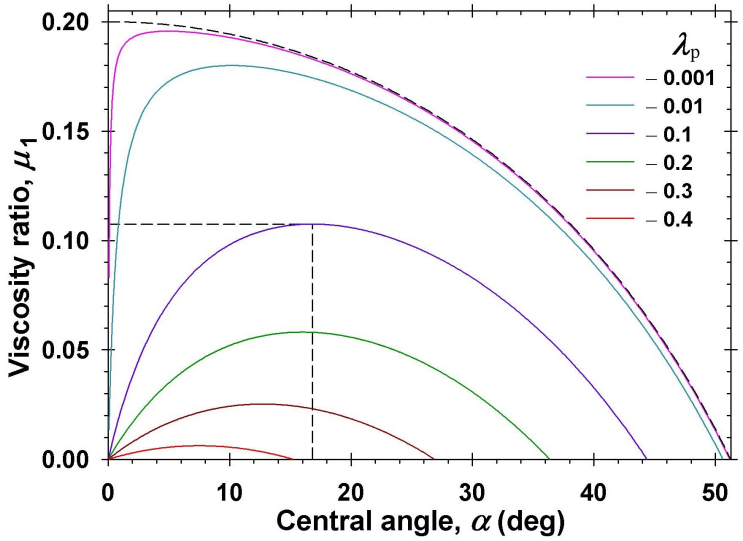

Figure 3.2: Lines with fixed values of the singularity parameter, λ_p.

3.4 Numerical results

The problem (3.8)–(3.21) is solved by introducing numerical time and using the D'Yakonov scheme (see Chapter 2). In Table 3.1, we validate the results by comparing the values of the drag coefficient, calculated via the proposed method, to the semi-analytic results [3.1] for $\alpha \leq 90^\circ$ and fluid–air interface. The computations are performed for $\delta_\sigma = 0.017$, $\delta_\tau = 0.05$ and different time steps δ_t. The relative error is less than 1% and the CPU time on a laptop with processor Intel Core i5-4200H is less than 10 s in all of the studied cases. Fig. 3.3 shows the pressure distribution for air/water interface for two different values of the three-phase

Table 3.1: Comparison between the calculated values, using the proposed method, and analytic values of the drag force coefficient [3.1].

α (°)	δ_t	CPU time (s)	appr. drag coeff.	exact drag coeff.	Rel. error (%)
15	0.10	2.534	1.4306	1.4374	0.473
30	0.15	7.332	1.4013	1.3392	0.612
60	0.45	7.504	1.2522	1.2509	0.104
75	0.60	5.242	1.1473	1.1370	0.906
90	0.60	8.798	0.9916	1.0000	0.840

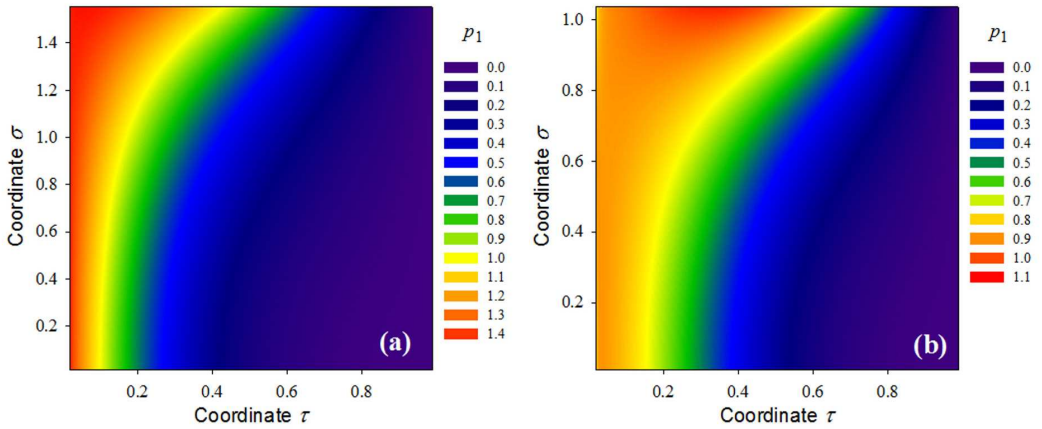

Figure 3.3: Pressure distribution for air–fluid interfaces: (a) $\alpha = 90°$; (b) $\alpha = 60°$.

contact angle. It is well illustrated that the pressure maximum for $\alpha = 90°$ is at the contact line, while that for $\alpha = 60°$ is shifted along the particle surface inside the fluid phase. The proposed algorithm decreases the computational time from 10 to 1000 times, compared to that in [3.2]. The smaller the contact angle is, the faster the proposed approach is.

3.5 Conclusion

The hydrodynamic problem for translation of a spherical particle, attached to a fluid–fluid interface, is simplified by using the gauge formulation, introduction of appropriate functions and toroidal coordinates, which reduces the three-dimensional Stokes equations to a two-dimensional system of eight homogeneous partial differential equations. The problem is solved, using the D'Yakonov method and reformulating adequately the boundary conditions. As a result, the numerical time is reduced from 10 to 1000 times, compared to that in [3.2]. From practical viewpoint, these calculations are essential for determination of contact angle of micron particles and for solving two-dimensional crystallization problem.

References

[3.1] M. Zabarankin, *Proc. R. Soc. A* 463, 2329–2349 (2007).
[3.2] K. Danov, R. Dimova, B. Pouligny, *Phys. Fluids* 12, 2711–2722 (2000).

4. Motion of long bubbles in gravity- and pressure-driven flow through cylindrical capillaries up to moderate capillary numbers

4.1 Literature overview

The transport of bubbles and drops through capillaries and porous media plays an important role in many technological and biological systems: enhanced oil recovery; movement of red blood cells; pulmonary airway reopeninig; motion of discrete bubbles in porous materials; biomechanics and microfluidic devices; circulating fluidized bed devices; etc. In some of these applications (e.g. microfluidics), the dimensionless thickness of the liquid film, h, is an important design parameter and, therefore, it is essential to find an expression for it.

In the current work, we study the motion of long bubbles in the gravity- and pressure-driven flows thought cylindrical capillaries. Most of the research considers the two effects separately and their interplay is not described systematically [4.1]. Therefore, it is convenient to study two simplified cases of the motion of bubbles and drops: in vertical capillaries, sealed at one end, under the action of gravity; in horizontal tubes through which a fluid is flowing. Bretherton solved the two simplified cases by using the lubrication approximation for the flow in the thin layer between the bubble and the capillary [4.2]. Then, he matched the lubrication approximation with the radius of curvature of the bubble front, corresponding to the capillary radius. The obtained asymptotic expressions are accurate to within 10% for small capillary numbers Ca ($Ca < 5.0 \times 10^{-3}$) in the case of pressure-driven flows and for Bond numbers in the interval $(0.842,\ 1.04)$ in the case of gravity-driven flows. In 2014, using the Bretherton approach and matching the lubrication approximation solution with more realistic radius of curvature at the bubble front, Klaseboer et al. [4.3] derive theoretically an extended expression for dimensionless thickness, which is valid for $Ca < 2$ in the case of pressure-driven flows.

To extend the region of validity of Bretherton model [4.2], Ratulowski and Chang [4.4] considered the lubrication solution in cylindrical coordinates. To avoid the ill-defined procedure of matching the lubrication approximation solution with the bubble shape at its front [4.2, 4.3], the normal stress boundary condition, written in terms of an arc length of the bubble surface, is used in order to solve the respective boundary value problem for the film thickness at the cylindrical part of the bubble, h, in [4.4]. This approach leads to a good theoretical description of the experimental data for the relative increase in the velocity, W, for up to 40 times larger capillary numbers ($Ca < 0.2$) than the applicability region of the Bretherton formula but still further improvements are needed to explain the significant deviations at higher capillary numbers. In this work, we generalized the approach, proposed by Ratulowski and Chang, by keeping not only the zero-order but also the first-order terms in the lubrication approximation. This method leads to sufficient improvement in the accuracy. Moreover, this approach is valid for moderate capillary and Bond numbers and could

be generalized by introducing complex interfacial rheology and intermolecular forces.

4.2 Mathematical model

Let us consider a cylindrical capillary of radius R, filled with incompressible Newtonian fluid with dynamic viscosity η and density ρ. Inside the fluid, there is an axisymmetric bubble with an axis of revolution, coinciding with the axis of revolution of the capillary. The bubble moves with velocity V_b, parallel to the tube wall, under the action of the Poiseuille flow and of gravity with acceleration $\mathbf{g}$ (see Fig.4.1). The surface of the bubble is a fully mobile (the shear stress at the bubble surface is zero) or a tangentially immobile surface (the immobile surface acts as a solid surface).

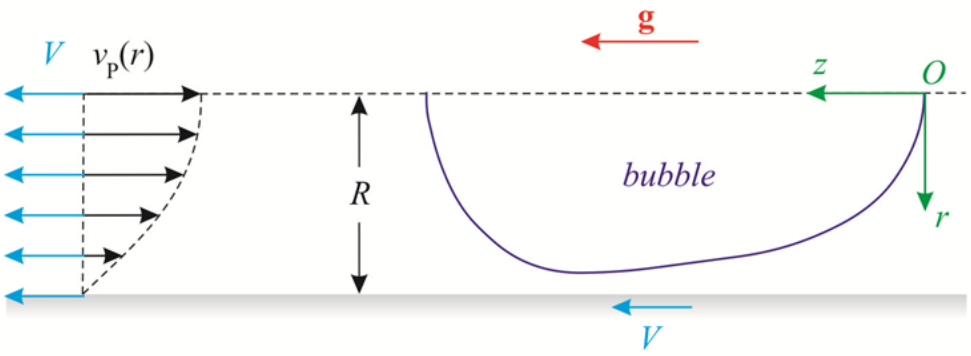

Figure 4.1: An axisymmetric bubble moves in a cylindrical capillary of radius R under the action of gravity and Poiseuille flow.

We introduce a cylindrical coordinate system (r, φ, z) with a center at the bubble apex and axis of revolution Oz, pointing in a direction, opposite of the bubble motion (see Fig. 4.1). First, the problem is axisymmetric and, therefore, the variables depend only on r and z. Thus, we shall consider the problem in the r-z plane only. Second, due to the fact this coordinate system is fixed at the bubble apex, the translational velocity of the bubble is equal to zero and the capillary wall and the whole fluid translate along axis Oz with velocity V_b.

We scale the mean curvature, the radial and axial coordinates of the bubble with the capillary radius R, the velocity components — with the bubble velocity V_b and the pressure — with $\eta V_b/R$. The effects of buoyancy and capillary forces are measured, using the Bond number, Bo, the capillary numbers, Ca and Ca_{pm}, and the relative increase in the velocity, W:

$$Bo = \frac{\rho g_z R^2}{\sigma}, \; Ca = \frac{\eta V_b}{\sigma}, \; Ca_{pm} = \frac{\eta V_{pm}}{\sigma}, \; W = 1 - \frac{V_{pm}}{V_b}, \tag{4.1}$$

where g_z is the z-component of the gravity $\mathbf{g}$, σ is the surface tension of the bubble and V_{pm} is the mean speed of the Poiseuille flow.

We model the fluid motion, using the Stokes equations. Then, the dimensionless radial

component u and axial component v of the fluid velocity satisfy the equations

$$\frac{1}{r}\frac{\partial}{\partial r}(r\,u)+\frac{\partial v}{\partial z}=0, \tag{4.2}$$

$$\frac{\partial p}{\partial r}=\frac{\partial}{\partial r}\left[\frac{1}{r}\frac{\partial}{\partial r}(r\,u)\right]+\frac{\partial^2 u}{\partial z^2}, \tag{4.3}$$

$$\frac{\partial p}{\partial z}=\frac{1}{r}\frac{\partial}{\partial r}\left(r\frac{\partial v}{\partial r}\right)+\frac{\partial^2 v}{\partial z^2}+\frac{Bo}{Ca}. \tag{4.4}$$

Next, we describe the bubble surface as $r=r_b(s),\ z=z_b(s)$, where r_b and z_b are the radial and the axial coordinates of the bubble surface and s is the arc length of S, measured from the bubble apex. Using geometric considerations, the bubble surface S is modelled as

$$\frac{dr_b}{ds}=\cos\theta, \tag{4.5}$$

$$\frac{dz_b}{ds}=\sin\theta, \tag{4.6}$$

$$2H=\frac{d\theta}{ds}+\frac{\sin\theta}{r_b}, \tag{4.7}$$

where θ is the meniscus running slope angle and H is the dimensionless mean curvature. In order to close the considered problem, we apply the following boundary conditions:

- no-slip boundary conditions at the capillary wall:

$$u=0,\ v=1 \text{ at } r=1; \tag{4.8}$$

- inlet/outlet boundary conditions at infinity:

$$u=0,\ v=1+v_p(r) \text{ at } |z|\to\infty, \tag{4.9}$$

  where $v_p(r)$ is the axial coordinate of the Poiseuille velocity profile;

- simple flow rate boundary condition:

$$2\int_{r_b}^{1} rv\,dr=W; \tag{4.10}$$

- tangential stress boundary condition at the bubble surface:

$$\cos(2\theta)\left(\frac{\partial v}{\partial r}+\frac{\partial u}{\partial z}\right)+\sin(2\theta)\left(\frac{\partial v}{\partial z}-\frac{\partial u}{\partial r}\right)=0 \text{ at } S; \tag{4.11}$$

- normal stress boundary condition at the bubble surface:

$$p_b=p-2\sin^2\theta\left[\cot^2\theta\frac{\partial v}{\partial z}+\frac{\partial u}{\partial r}-\cot\theta\left(\frac{\partial v}{\partial r}+\frac{\partial u}{\partial z}\right)\right]+\frac{2H}{Ca} \text{ at S.} \tag{4.12}$$

For free surfaces, the problem consists of Eqs. (4.2)–(4.12). In the case of a tangentially immobile bubble surface, Eq. (4.11) is replaced by the conditions for surface solidification:

$$u = 0,\ v = 0 \text{ at S} \tag{4.13}$$

and the normal boundary condition is simplified as follows:

$$p_b = p + \frac{2H}{Ca} \text{ at S.} \tag{4.14}$$

We assume that the characteristic dimensionless thickness of liquid layer, ε, far from the bubble apex is a small parameter of the considered problem and, therefore, rescale the radial coordinate, r, as follows:

$$r = 1 + \varepsilon\xi. \tag{4.15}$$

The expansions in series for the radial and the axial components of the fluid velocity and for the pressure with respect to the small parameter, ε, are sought-out in the following form:

$$u = \varepsilon\tilde{u}_0 + \varepsilon^3\tilde{u}_2 + O\left(\varepsilon^4\right),\ v = \tilde{v}_0 + \varepsilon^2\tilde{v}_2 + O\left(\varepsilon^3\right),\ p = \frac{\tilde{p}_0}{\varepsilon^2} + \tilde{p}_2 + O\left(\varepsilon\right). \tag{4.16}$$

One substitutes the expansions (4.15)–(4.16) in the Stokes problem (4.2)– (4.4), closed with the no-slip (4.8), the simple flow rate (4.10) and the tangential boundary condition (4.11) or (4.13). Equating the leading coefficients in each of the equations, we obtain a system of partial differential equations with boundary conditions. Its solution, the zero-order approximations for the flow variables u, v and p, is found analytically. Analogously, one gets the first-order approximations for the flow variables. Next, these approximations are substituted in the normal stress boundary condition and the following nonlinear system of four ordinary differential equations for r_b, z_b, θ and the dynamic pressure difference p_s:

$$\frac{dr_b}{ds} = \cos\theta, \tag{4.17}$$

$$\frac{dz_b}{ds} = \sin\theta, \tag{4.18}$$

$$\frac{d\theta}{ds} = -Ca\,p_s - \frac{\sin\theta}{r_b}, \tag{4.19}$$

$$\frac{dp_s}{ds} = F\left(r_b, \theta, p_s, Bo, Ca_{pm}\right). \tag{4.20}$$

is obtained. Using small perturbations around the cylindrical shape of the bubble, the initial conditions for the problem in the case of long bubbles acquire the form

$$r_b(s_{in}) = r_c - \delta,\ z_b(s_{in}) = z_{in}, \tag{4.21}$$

$$\theta(s_{in}) = \frac{\pi}{2} + \lambda\delta,\ p_s(s_{in}) = -\frac{1}{Ca\,r_c} - \left(\lambda^2 + \frac{1}{r_c^2}\right)\frac{\delta}{Ca}, \tag{4.22}$$

where r_c is the radius of the cylindrical part of the bubble, δ is the initial value of the shape perturbation and λ is the real root of the equation

$$(\lambda\,r_c)^3 + \lambda\,r_c + a = 0. \tag{4.23}$$

In the latter, a is computed as follows:

$$a = \begin{cases} \dfrac{2r_c^2\left[8Ca_{pm} + Bo\left(1 - r_c^4 + 4r_c^4 \ln r_c\right)\right]}{1 - 4r_c^2 + 3r_c^4 - 4r_c^4 \ln r_c} & \text{for free surface;} \\ \dfrac{r_c^2\left(1 - r_c^2 + 2r_c^2 \ln r_c\right)\left[8Ca_{pm} + Bo\left(1 - r_c^2\right)^2\right]}{\left(1 - r_c^2\right)^2\left[r_c^2 - 1 - \left(1 + r_c^2\right)\ln r_c\right]} & \text{for tangentially immobile surface.} \end{cases} \tag{4.24}$$

4.3 Regions of validity of parameters

Due to the fact that long bubbles appear only if $a > 0$, we check when the expressions (4.24) are positive for $0 < r_c < 1$ and $Ca > 0$. The obtained constraints for the ratio Ca_{pm}/Bo in the case of free or immobile surfaces are shown in Fig. 4.2. Note that the problem has no solution for parameter values in the region, enclosed by the solid line ($Ca = 0$) and the dashed line ($a = 0$).

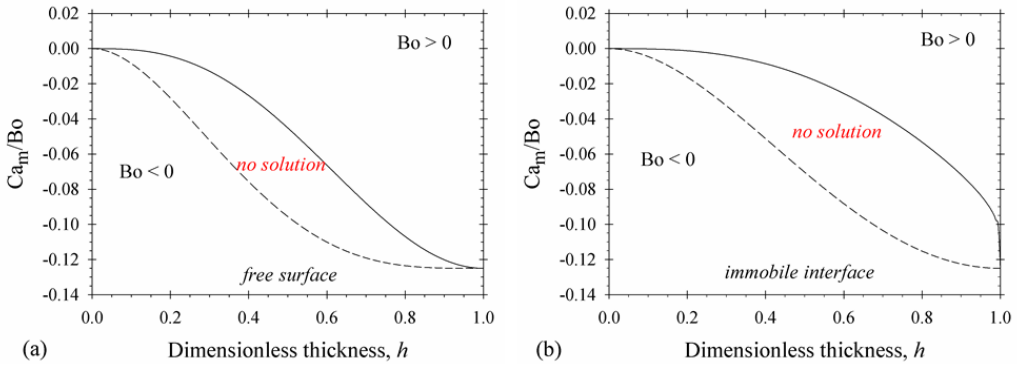

Figure 4.2: Regions of physical parameters for possible elongated bubble profiles in the case of free or tangentially immobile surface. Solid lines correspond to $Ca = 0$ and dashed lines — to $a = 0$.

4.4 Numerical results

Generally speaking, the system (4.17)– (4.20) models the form of a drop for a given pressure distribution along the bubble surface. The solution depends on the initial conditions and describes different types of possible capillary profiles: open or closed capillary curves, curves with loops, etc (see Fig. 4.3). For example, in the case of a free surface, $Bo = 2$ and $Ca_{pm} = 0$, the capillary curve has a loop for $h = 0.1$, the calculated profile is open for $h = 0.2$, and only for $h = 0.1617$, one obtains the real bubble shape (Fig. 4.3a). Analogously, for $Bo = 0$ and $Ca_{pm} = 0.5$ in the case of free surfaces, the capillary profiles are open for $h = 0.26$ and $h = 0.29$ and the physical solution is obtained for $h = 0.2752$ (Fig. 4.3b). These experiments show the variety of the problem solutions but we are interested only in the physical solution, which corresponds to a closed bubble profile. For given parameters Bo and Ca_{pm}, it is computed by varying the dimensionless thickness, h, so that one obtains a closed profile.

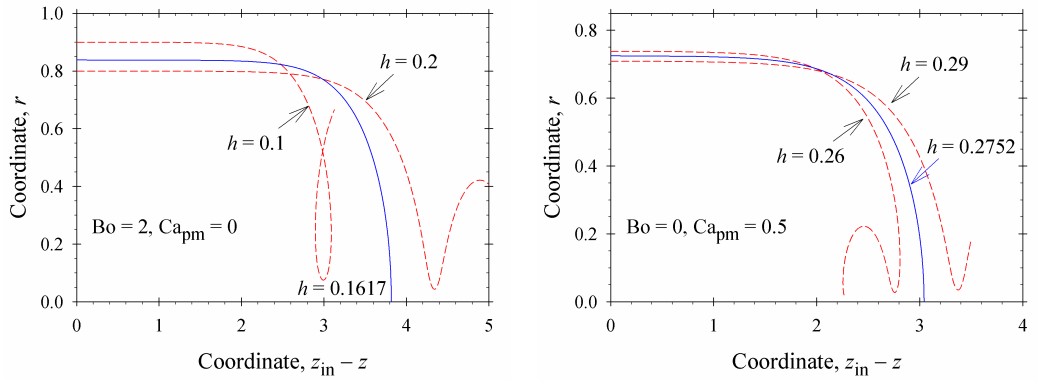

(a) $Bo = 2$, $Ca_{pm} = 0$. (b) $Bo = 0$, $Ca_{pm} = 0.5$.

Figure 4.3: Calculated capillary profiles for three different values of the dimensionless layer thickness, h, in the case of a free bubble surface.

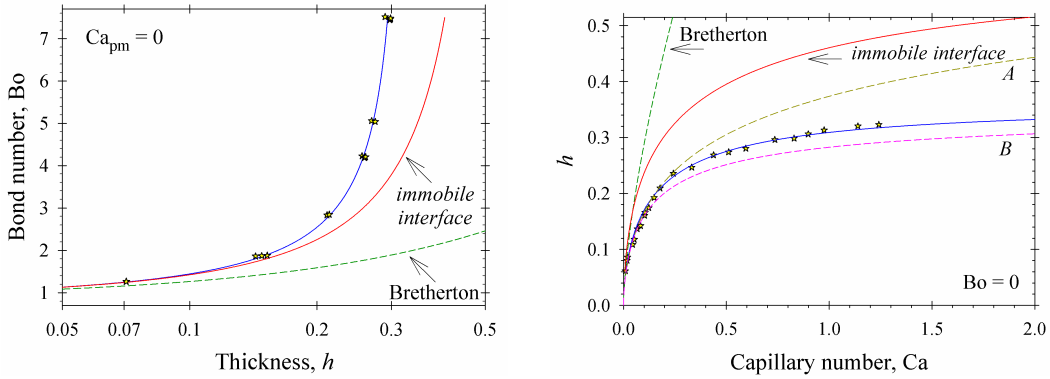

(a) Rising bubbles. (b) Taylor bubbles.

Figure 4.4: Comparison between experimental data [4.5–4.7] (symbols) and the theoretical calculations. Solid line — generalized lubrication approximation; A-line — model, based on the zero-order lubrication approximation [4.4]; B-line — extended Bretherton model [4.3].

4.4.1 Comparison with experimental data and theoretical results

Fig. 4.4a shows experimental data [4.5] (symbols) for the dimensionless layer thickness of a long rising bubble in capillary as function of the Bond number ($Ca_{pm} = 0$). The calculations for a free surface (solid blue line) describe excellently the experimental data for all studied values of the Bond number ($Bo \leq 7.5$). The Bretherton asymptotic formula [4.2] (dashed line in Fig. 4.4a) gives good results for low values of the capillary number, $Ca < 3.2 \times 10^{-4}$.

In the case of motion of long bubbles under the action only of the Poiseuille flow ($Bo = 0$), the comparison between experimental data and numerical calculations are shown in Fig. 4.4b. The original Bretherton asymptotic solution [4.2] (dashed line) describes experimental data with accuracy of 10% for low values of the capillary numbers $Ca < 5 \times 10^{-3}$. The extended Bretherton model [4.3] (B-line) gives acceptable results for $Ca < 0.1$. The

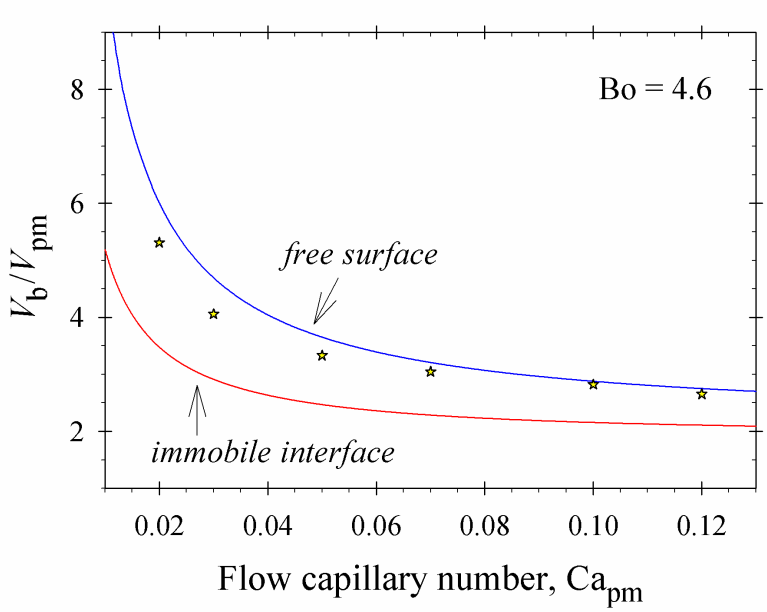

Figure 4.5: Comparison between experimental data [4.1] (symbols) for relative velocity $V_b/V_{pm} > 0$ of long bubbles and the theoretical calculation for fully mobile and immobile interfaces for fixed Bond number, $Bo = 4.6$.

model [4.4] (A-line), based on the zero-order lubrication approximation, describes well the experimental data for $Ca < 0.2$. The use of the generalized lubrication approximation, which accounts also for the first-order lubrication approximation, leads to an excellent description of the experimental data for $Ca < 2.0$, see Fig. 4.4b.

Fig. 4.5 shows a comparison between experimental data and theoretical calculations for the relative velocity V_b/V_{pm} in the case of simultaneous action of the Poiseuille flow and gravity. The experimental data [4.1] (symbols) are close to the theoretical calculations for bubbles with free surfaces. The small deviations of the experimental data from the calculated theoretical line in the case of a bubble with free surface are likely due to trace amounts of surface-active contaminations in the working fluid [4.1].

4.4.2 Simultaneous action of the Poiseuille flow and gravity

In the literature, there are no systematic experimental data for the long bubble motion under simultaneous action of the Poiseuille flow and gravity (like those illustrated in Fig. 4.5). Fig. 4.2 shows that one distinguishes two general cases. The first one corresponds to $Bo > 0$, when the Poiseuille flow accelerates the bubble motion for $Ca_{pm} > 0$ and decelerates it for $Ca_{pm} < 0$. The experimental data in Fig. 4.5 correspond to $Bo > 0$ and $Ca_{pm} > 0$. Fig. 4.6 summarizes the numerical results for the effect of the Poiseuille flow on the thickness of cylindrical film layer for positive values of the Bond number and different models for surfaces (fully mobile and tangentially immobile). The greater values of the threshold Bond number are interrelated with the increase of the thicknesses of wetting films in cylindrical parts (Fig. 4.6). Oppositely for $Ca_{pm} > 0$, very thin cylindrical liquid layers can be realized. As

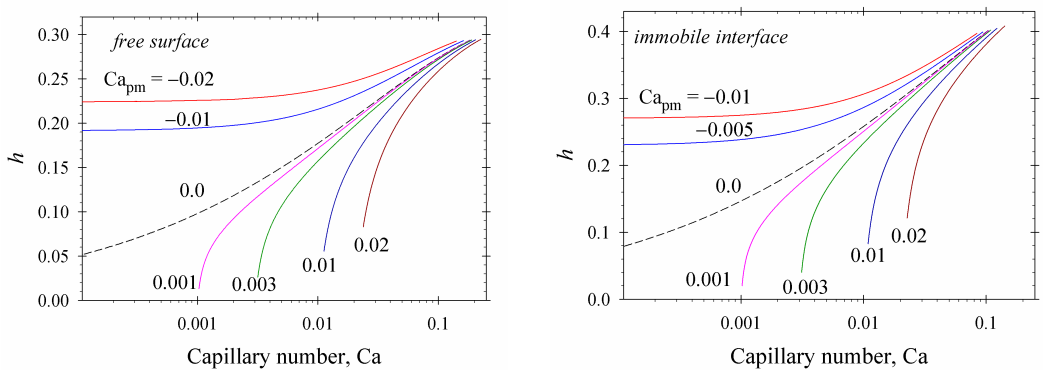

(a) Free surfaces. (b) Tangentially immobile interfaces.

Figure 4.6: Effect of the Poiseuille flow on the thickness of cylindrical film layer.

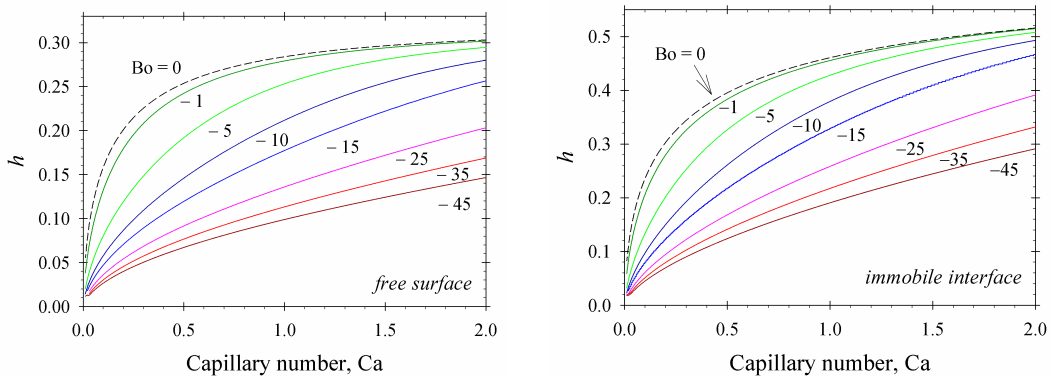

(a) Free surface model. (b) Tangentially immobile surfaces.

Figure 4.7: Effect of gravity on the bubble translational velocity and on the thickness of cylindrical film layer, h, in the presence of Poiseuille flow.

it can be expected, the films for tangentially immobile interfaces are thicker than those for fully mobile surfaces.

The second general case is when the gravity decelerates the bubble motion ($Bo < 0$ and $Ca_{pm} > 0$, see Fig. 4.2). The numerical results for the dependence of h on the capillary number, Ca, for both types of bubble interfaces are summarized in Fig. 4.7. The increase in the magnitude of Bond number, $|Bo|$, decreases the thickness of the wetting cylindrical film. Moreover, the bubbles with tangentially immobile interfaces move with the same translational velocity as those with free surfaces under the action of more intensive Poiseuille flow.

4.5 Conclusion

We studied the motion of long axisymmetric bubbles with free and tangentially immobile interfaces through capillaries, based on the exact solution of the hydrodynamic problem in cylindrical coordinate system in the frame of the generalized lubrication approximation, keeping the zero-order terms [4.4] and the first-order terms. As a result the expressions for the fluid velocity and dynamic pressure are calculated for an arbitrary shape of the bubble. These quantities are substituted in the normal stress boundary condition to obtain the boundary value problem in terms of an arc length for the bubble shape. Diagrams for the necessary conditions for the appearance of long bubbles are constructed (Fig. 4.2). The implemented method allows fast and precise calculation of the dependence of the capillary number and the wetting film thickness in the cylindrical part on the system parameters.

The comparisons with available experiments (Figs. 4.4 and 4.5) show the validity of the proposed approach for moderate capillary, Ca, and Bond, Bo, numbers ($Ca < 2$ and $Bo < 7.5$). When the pressure-driven flow hinders the rising of bubbles, the gravity should be sufficiently high to ensure bubble motion (Fig. 4.6). A very low applied pressure gradient in the opposite direction of bubble translation leads to bubble motion and the Bretherton condition ($Bo > 0.842$) does not take a place. When the gravity opposes the pressure-driven bubble motion (Fig. 4.7), the translational velocity decreases for high absolute values of the Bond number. Generally, in the case of tangentially immobile interfaces, the translational velocity, V_b, is lower and the wetting film thickness, h, is higher than those, predicted for free bubble surfaces at given fixed system parameters.

References

[4.1] A. Borhan, J. Pallinti, *Ind. Eng. Chem. Res.* 37, 3748–3759 (1998).
[4.2] F. Bretherton, *J. Fluid Mech.* 10, 166–188 (1961).
[4.3] E. Klaseboer, R. Gupta, R. Manica, *Phys. Fluids* 26, 032107 (2014).
[4.4] J. Ratulowski, H.-C. Chang, *Phys. Fluids A - Fluid* 1, 1642–1655 (1989).
[4.5] H. Goldsmith, S. Mason, *J. Fluid Mech.* 14, 42–58 (1962).
[4.6] G. Taylor, *J. Fluid Mech.* 10, 161–165 (1961).
[4.7] P. Aussillous, D. Quéré, *Phys. Fluids* 12, 2367–2371 (2000).

5. Conclusions and main contributions

5.1 General conclusions

In the literature [5.1, 5.2], the problem for the electrostatic distribution is solved numerically and analytically (in the terms of Mehler–Fock integral transform) in the case of one fully conductive bulk phase (water). This simplification leads to the Dirichlet boundary conditions at the particle–water and dielectric phase–water boundaries (the electrostatic potential at these boundaries is equal to zero). The estimation of the part of the electro-dipping force, arising from the water phase, shows that the contribution from the water phase is not negligible and one should account for all dielectric phases simultaneously. In Chapter 2, the Laplace equations for the electrostatic potentials in all three domains (spherical particle, upper and lower dielectric phases) are solved with the boundary conditions at all three dividing surfaces (continuity of the electrostatic potentials and balance of surface charges). The numerical solution of this generalized (in fact more realistic) problem gives the answer to the question for the role of water phase on the electrostatic potential distribution. In the most cases, some of the physical quantities have weak singularities at the three-phase contact line (in our case, the derivative of the electrostatic potential that is the electric field vector). Physically, a weak singularity means that the integral of the respective force, containing these quantities, over the surface has a well-defined finite value. The isolation of the weak singularity, transformation of the complex numerical domains into rectangles, using toroidal coordinates, and the application of fast and precise numerical methods become of a crucial importance for the adequate solution of the problem, described in Chapter 2.

From a physical viewpoint, the formulation of the model in Chapter 3 is quite clear: Stokes equation in each of the incompressible fluid phases; continuity of the velocity and tangential stresses at the flat dividing surface between them; given translational velocity of the spherical colloidal particle, attached to the interface, with a fixed three-phase contact angle. One possible numerical approach to solve the problem is the two-vorticities-one-velocity formulation [5.3]. The reported method is of a second-order in the three-dimensional domains (with respect to the Stokes equations) but of a first-order in the two-dimensional domains (with respect to the boundary conditions). As a result, the method is slow and not convenient for multitask applications. The problem has also an analytical solution in terms of the Mehler–Fock integral transform for negligible viscosity of one of the fluids (e.g. water–air interface) and contact angles $\leq 90^\circ$ [5.4]. In fact, this particular case is not realistic and with a quite restricted application. Nevertheless, the only way to check the validity of a numerical method and its precision is to use this exact solution of the problem. The main reason for the difficulties in numerical computations in [5.3] and for the restricted validity of the analytical solution (contact angles $\leq 90^\circ$) [5.4] is the weak singularity of the pressure function at the three-phase contact line.

Our approach in Chapter 3 is based on the gauge reformulation of the Stokes problem, which introduces vector and scalar potentials of the velocity and pressure distributions; the reduction of the three-dimensional problem in the two-dimensional one for the first Fourier modes with respect to the polar angle; the transformation of the complex domains

into rectangles, using a modification of the standard toroidal coordinates. As a result, the original problem for the bulk fluids is reduced to a system of four partial differential equations of a second-order for each of the phases. These systems are interrelated with the boundary conditions at the dividing surfaces. The main difficulty in the gauge formulation is to introduce self-consistent boundary conditions for the vector and scalar potentials. The introduced in Chapter 3, new type of boundary conditions resolves this problem and gives possibility to construct an efficient second-order ADI-type scheme for the numerical solution, which is fast enough and gives good precision. The asymptotic analysis of the weak singularity at the three-phase contact line shows the regions of regular and singular pressure distributions and improves the precision of the calculation for the drag force.

In Chapter 4, we combine the Bretherton idea with the approach in [5.5] and solve the hydrodynamic problem for the lubrication approximation not only for the zero-order but also for the first-order approximation of the fluid velocity and pressure. As it can be expected, this increases the precision of the used approximation solution. One advantage of this analytical method is its validity for an arbitrary smooth shape of the interface. As a result, the analytical expressions for the flow characteristics in the case of tangentially mobile and immobile interfaces are obtained. The normal stress boundary condition, in which the lubrication approximation solution is substituted, defines the shape of bubble. The obtained numerical problem is a system of four nonlinear differential equations with one adjustable parameter, which has to be varied in order to calculate a close capillary profile. From mathematical and numerical viewpoint, the obtained problem is analogous to the method known as an axisymmetric drop shape analysis, which is incorporated in many commercial apparatuses for measurement of the surface tension and the contact angle. The obtained numerical results describe excellently the available experimental data; expand the validity of the semi-analytical model by at least two orders of magnitude to moderate capillary and Bond numbers; explain the complex behavior of the simultaneous action of gravity and pressure-driven flow; show the principle difference between mobile and immobile interfaces.

5.2 Main contributions

1. The problem for distribution of electrostatic potentials in dielectric media (two immiscible fluid phases and a spherical colloidal particle, attached to the flat interface between them) consists of Laplace equations for the functions in the three-dimensional domains, continuity of these functions and conditions for their normal derivatives at the known two-dimensional boundaries. The problem is solved numerically, using the developed for this purpose fast and efficient algorithm. The strategy of computations is based on: the transformation of the complex domains into rectangles, using appropriate toroidal coordinates; analytical computation of the weak singularity at the three-phase contact line; implementation of a self-consistent second-order ADI-type numerical scheme. The results generalize the idealized case in [5.1], in which the water permeability is assumed to be infinite. In the present study, we take into account its finite value as well as the simultaneous effect of all dielectric phases.

2. The problem for the translational motion of a spherical colloidal particle, attached to a flat interface between two incompressible fluids, consists of Stokes equations for the velocity vector and the pressure (in fact bi-Laplacian of the velocity vector is equal to zero) in the three-dimensional domains, continuity of the velocity and the tangential stresses at the two-dimensional fluid–fluid interface and a known velocity vector at the particle surface. The problem is solved numerically from 10 to 1000 times faster than by the proposed

method in method [5.3]. The strategy of computations is based on: the gauge formulation in terms of vector and scalar potentials of velocity and pressure; transformation of the three-dimensional problem into the two-dimensional one for the first Fourier mode with respect to the polar angle; transformation of the complex domains into rectangles, using modified toroidal coordinates; construction of a second-order ADI-type numerical scheme, taking into account the original formulation of the two-dimensional boundary conditions; the analytical calculation of the weak singularity at the three-phase contact line and the isolation of the pressure singularity, which increases the precision of the drag force calculations.

3. The problem for the gravity- and pressure-driven motion of a long bubble with tangentially mobile (classical case) or immobile interface (biological membrane, surfactant laden interface, etc.) through a cylindrical capillary is solved semi-analytically. The problem consists of: Stokes equations in the three-dimensional domain; known Poiseuille velocity profile at large distances from the bubble; no-slip boundary condition at the capillary wall; tangential and normal stress boundary conditions at the deformable bubble surface. The strategy of computations is based on: the exact analytical solution of the Stokes problem for small slopes of the tangent to the bubble shape, which leads to zero- and first-order approximations at an arbitrary smooth bubble shape; substitution of the obtained solutions in the normal stress boundary condition, from which it follows a system of four first order nonlinear differential equations with respect to the arc length with one adjustable parameter (the capillary pressure at the bubble apex); the efficient numerical scheme for calculating the fourth-order boundary value problem for the shape by fitting the adjustable parameter in order to obtain a closed capillary profile. As a result, the obtained method describes excellently the available experimental data, increases more than two orders of magnitude the range of the applicability of the analytical approaches known in the literature, and explain the complex physical picture of the simultaneous action of gravity and pressure-driven flows for classical and tangentially immobile interfaces.

References

[5.1] K. Danov, P. Kralchevsky, *J. Colloid Interface Sci.* 298, 213–231 (2006).

[5.2] P. Petkov, K. Danov, P. Kralchevsky, *Journal of Colloid and Interface Science* 462, 223–234 (2015).

[5.3] K. Danov, R. Dimova, B. Pouligny, *Phys. Fluids* 12, 2711–2722 (2000).

[5.4] M. Zabarankin, *Proc. R. Soc. A* 463, 2329–2349 (2007).

[5.5] J. Ratulowski, H.-C. Chang, *Phys. Fluids A - Fluid* 1, 1642–1655 (1989).

6. Dissemination of dissertation results

6.1 List of publications

1. G. Lyutskanova-Zhekova, K. Danov, Effect of Ionic Strength on the Electro-dipping Force. In Proceedings of the 9th International conference on Numerical Methods and Applications NMA, Borovets, Bulgaria, 20–24 August 2018; Lecture Notes in Computer Science Volume, SJR: 0.427 (2019). DOI: 10.1007/978-3-030-10692-8_49.

2. G. Lyutskanova-Zhekova, K. Danov, Motion of a spherical particle attached to the interface between two viscous fluids, Progress in Industrial Mathematics (2019). DOI: 10.1007/978-3-030-27550-1_12.

3. K. Danov, G. Lyutskanova-Zhekova, S. Smoukov, Motion of long bubbles in gravity- and pressure-driven flow through cylindrical capillaries up to moderate capillary numbers, Physics of fluids **33** (2021), no. 11, IF: 4.980, Quartile: Q1. DOI: `https://doi.org/10.1063/5.0070619`.

6.2 List of citations of the publications

G. Lyutskanova-Zhekova, K. Danov, Effect of ionic strength on the electro-dipping force. In: G. Nikolov, N. Kolkovska, K. Georgiev (Eds.), Numerical Methods and Applications. LNCS 11189, Springer, 2019, 433–440.

Citations(1):

1. V. Lotito, M. Karlusic, N. Jaksic, K.T. Luketic, U. Muller, T. Zambelli, S. Fazinic, Shape deformation in ion beam irradiated colloidal monolayers: An AFM investigation, Nanomaterials **10** (2020), no. 453.

K. Danov, G. Lyutskanova-Zhekova, S. Smoukov, Motion of long bubbles in gravity- and pressure-driven flow through cylindrical capillaries up to moderate capillary numbers, Physics of fluids **33** (2021), no. 11, IF: 4.980, Quartile: Q1. DOI: `https://doi.org/10.1063/5.0070619`.

Citations(2):

1. B. Monnet, M. Christopher, V. Vidal et al., Bubble rise in a Hele-Shaw cell: bridging the gap between viscous and inertial regimes, July 2022, Journal of Fluid Mechanics 942, DOI: 10.1017/jfm.2022.361.

2. Z. Zhu, H. Liu, H. Ding, Buoyancy-driven bubbles in a constricted vertical capillary, March 2022, Physics of Fluids 34(3):032102, DOI: 10.1063/5.0083160.

6.3 List of reports, presented by the author:

1. "Motion of spherical particle attached to the interface between two viscous fluids", report at the international conference "20th European Conference on Mathematics for Industry", 18-22 June 2018, Budapest, Hungary.

   Link to the conference website: https://ecmi.bolyai.hu/

2. "Axisymmetric equilibrium shapes of single-wall carbon nanotubes under pressure", report at the international conference BIOMATH 2018, 24-29 June 2018, Sofia, Bulgaria.

   Link to the conference website: http://www.biomath.bg/2018/

3. "Effect of ionic strength on the electro-dipping Force", report at the international conference NM&A'18, 20-24 August 2018, Borovets, Bulgaria.

   Link to the conference website: https://nma18.fmi.uni-sofia.bg/

4. "Motion of spherical particle attached to the interface between two viscous fluids" (in Bulgarian), Spring scientific session of the Faculty of Mathematics and Informatics of the Sofia University "St. Kliment Ohridski", 16 March 2019, Sofia, Bulgaria. Link to the conference website:
   https://www.fmi.uni-sofia.bg/bg/proletna-nauchna-sesiya-na-fmi-2019

5. "Generalized lubrication approach, applied to the Bretherton problem for motion of long bubbles in tubes", report at the international conference "Mathematics and its Applications", 4-10 August 2019, Novosibirsk, Russia.

   Link to the conference website: http://www.math.nsc.ru/conference/gsk/90/en/

6. "Differential equations of second and fourth order with applications in physicochemistry and biology", report at the scientific seminar of section "Mathematical Modelling and Numerical Analysis", 13 July 2020.

7. "Motion of long bubbles in gravity- and pressure-driven flow through cylindrical capillaries up to moderate capillary numbers", report at the international virtual conference "International conference on mathematical science", 7-9 October 2021, Surat, India.

   Link to the conference website:
   https://sites.google.com/view/icms2021/home?authuser=0